SUPPLEMENTAL MATERIAL

The analysis of P-SV converted phases presented in this paper was optimized to identify shallow intracrustal discontinuities by including high-frequency energy in the receiver function calculations and then separating the waveforms by backazimuth (e.g. Owens et al., 1984). Receiver functions were generated by deconvolving the vertical- component from the radial-component seismogram using the frequency-domain method (Langston, 1979). High signal-to-noise events were chosen for the analysis, and the low pre-event noise in the receiver functions indicates that the waveforms are not contaminated by processing artifacts. Different low-pass Gaussian filters (α=5.0 and 7.0, corresponding to maximum frequencies of ~2 Hz and ~3 Hz, respectively) were applied to evaluate waveform variation with frequency content. Gaussian values of 1.0-2.5 (yielding maximum frequencies of 0.1-1.0 Hz) are typically used in broadband studies of the lower crust and uppermost mantle. Higher-frequency receiver functions (α=7.0; up to 3 Hz) provide improved resolution at the expense of increased noise levels (Cassidy, 1992). In our forward models, interface depths were determined using P-SV delay times (Zhu and Kanamori, 2000), and the velocity models were based on P-SV polarities, constraints from surface geology, seismic reflection profiling, and laboratory measurements of shear-wave velocities (Vs). In the modeling, both Vp and Vs were allowed to vary. For additional information on the geologic interpretation of reflection profiles from the southern Appalachians, the reader is referred to Hatcher (1971), Coruh et al. (1987), Hatcher (1987), Phinney and Roy-Chowdhury (1989), Hatcher (1991), and Hatcher (2001).

The receiver-function gathers and corresponding bootstrapped stacks are shown in Figures DR1-DR7 and DR8-DR16, respectively. Bootstrap analysis was performed to evaluate the robustness of the vertically stacked conversions (Figs. DR8-DR16; Efron and Tibshirani, 1991). Stacked traces were corrected for moveout using a ray parameter of 0.06 s/km. In this study, the majority of earthquakes in the 30-95° epicentral range used for the analysis occurred in South America and the northern Pacific region (Fig. DR17; Table DR1). The approximate backazimuthal ranges used for the analysis were 150-180° and 275- 345° for South America and the northern Pacific, respectively. Suitable events from other regions (e.g. Atlantic mid-ocean ridge) were less numerous and generally yielded lower-quality receiver functions.

The analysis of high-frequency receiver functions separated by backazimuth is not always ideal for imaging deeper discontinuities because waveforms can vary significantly in regions characterized by lateral heterogeneity, dipping structure, or anisotropy (e.g. Levin and Park, 1997). In this study, the weak Moho P-SV conversions for some backazimuths (e.g. D04-NW; Fig. 3C) are attributed primarily to interference effects with unmodeled intracrustal multiples (e.g. Beck and Zandt, 2002). Lateral heterogeneity within the crust could cause these effects to vary with azimuth. Dipping structure or azimuthal anisotropy at the crust-mantle boundary remain a possibility, but these effects are difficult to assess because of the limited azimuthal event coverage for this region. Poor signal quality or a gradational Moho are also alternative explanations, but the strong PpPs multiples from the Moho observed on both backazimuths at some stations indicate that these causes are less likely.

In general, there is clear evidence for strong Moho conversions across the array when all backazimuths are considered, and the reader is referred to Parker et al. (2013) for lower-frequency ($\alpha = 2.5$) receiver-function stacks including events from both the S and NW

backazimuths. These data show the strong amplitude and continuity of Moho P- SV conversions across the crystalline southern Appalachians. Receiver functions showing strong Moho P-SV conversions (α = 1.0 and 2.0) from the Blue Ridge and Inner Piedmont are also presented in Baker and Hawman (2011).

REFERENCES CITED

Baker, M.S., and Hawman, R.B., 2011, Crustal structure in the southern Appalachians: A comparison of results obtained from broadband data and three-component, wide- angle P and S reflection data: Bulletin of the Seismological Society of America, v.101, p. 2796-2809, doi:10.1785/0120100341.

Beck, S.L., and Zandt, G., 2002, The nature of orogenic crust in the central Andes: Journal of Geophysical Research, v. 107, doi:10.1029/2000JB000124.

Cassidy, J.F., 1992, Numerical experiments in broadband receiver function analysis: Bulletin of the Seismological Society of America, v. 82, p. 1453-1474.

Coruh, C., Costain, J.K., Hatcher, R.D., Jr., Pratt, T.L., Williams, R.T., and Phinney, R.A., 1987, Results from regional vibroseis profiling: Appalachian ultra-deep core hole site study: Geophysical Journal of the Royal Astronomical Society, v. 89, p. 147-156, doi:10.1111/j.1365-246X.1987.tb04401.x.

Efron, B., and Tibshirani, R., 1991, Statistical data analysis in the computer age: Science, v. 253, p. 390-395, doi:10.1126/science.253.5018.390.

Hatcher, R.D., Jr., 1971, Stratigraphic, petrologic, and structural evidence favoring a thrust solution

to the Brevard problem: American Journal of Science, v. 270, p. 177- 202, doi:10.2475/ajs.270.3.177.

Hatcher, R.D., Jr., 1987, Tectonics of the southern and central Appalachian internides: Annual Review of Earth and Planetary Sciences, v. 15, p. 337-362, doi:10.1146/annurev.ea.15.050187.002005.

Hatcher, R.D., Jr., 1991, Interactive property of large thrust sheets with footwall rocks – the subthrust interactive duplex hypothesis: A mechanism of dome formation in thrust sheets: Tectonophysics, v. 191, p. 237-242, doi:10.1016/0040-1951(91)90059- 2.

Hatcher, R.D., Jr., 2001, Rheological partitioning during multiple reactivation of the Palaeozoic Brevard fault zone, southern Appalachians, USA, *in* Holdsworth, R.E., Strachan, R.A., Magloughlin, J.F., and Knipe, R.J., eds., The nature and tectonic significance of fault zone weakening: Geological Society of London Special Publication 186, p. 257-271, doi:10.1144/GSL.SP.2001.186.01.15.

Hatcher R.D., Jr., Lemiszki, P.J., Whisner, J.B., 2007, Character of rigid boundaries and internal deformation of the southern Appalachian foreland fold-thrust belt, *in* Sears J.W., et al., eds., Whence the Mountains? Inquiries into the Evolution of Orogenic Systems: A Volume in Honor of Raymond A. Price: Geological Society of America Special Paper 433, p. 243–276, doi:10.1130/2007.2433(12).

Langston, C.A., 1979, Structure under Mount Rainier, Washington, inferred from teleseismic body waves: Journal of Geophysical Research, v. 84, p. 4749-4762, doi:10.1029/JB084iB09p04749.

Levin, V., and Park, J., 1997, Crustal anisotropy in the Ural Mountains foredeep from teleseismic receiver functions: Geophysical Research Letters, v. 24, p. 1283-1286,

doi:10.1029/97GL51321.

Owens, T.J., Zandt, G., and Taylor, S.R., 1984, Seismic evidence for an ancient rift beneath the Cumberland Plateau, Tennessee: A detailed analysis of broadband teleseismic P waveforms: Journal of Geophysical Research, v. 89, p. 7783-7795, doi:10.1029/JB089iB09p07783.

Phinney, R.A., and Roy-Chowdhury, K., 1989, Reflection seismic studies of crustal structure in the eastern United States, *in*, Pakiser, L.C., and Mooney, W.D., eds., Geophysical framework of the continental United States: Boulder, Colorado, Geological Society of America Memoir 172, p. 613-653.

Zhu, L., and Kanamori, H., 2000, Moho depth variation in southern California from teleseismic receiver functions: Journal of Geophysical Research, v. 105, p. 2969- 2980, doi:10.1029/1999JB900322.

Figures DR1-DR7.

Receiver-function gathers showing P-SV conversion picks (gray bands) used to estimate depths shown in Figure 4. For each station, the Gaussian value (5.0 or 7.0) and backazimuth (s: south, nw: northwest) are shown in parentheses. The water level parameter used in the frequency-domain receiver function calculations (Langston, 1979) was 0.01.

Figure DR1.

Positive conversions from station D22 in the Valley & Ridge and stations D20 and D21 in the Blue Ridge show a southeastward increase in Grenville basement depth from 3.8 to

6.4 km, in agreement with estimates determined from seismic reflection profiling in this region (Hatcher et al., 2007). The upward decrease in shear-wave velocity beneath parts of the Valley and Ridge and Blue Ridge is interpreted to result from the dominance of low-velocity shale of the Rome Formation or Conasauga Group, rather than high-velocity quartzite or dolomite, overlying Grenville basement (Hatcher et al., 2007). This observation implies that receiver function conversion polarities may vary laterally depending on the lithology and thickness of platform assemblages above the basement surface.

Figure DR2.

For station D19, positive and negative conversions in receiver functions from the northwest and south backazimuths, respectively, are consistent with the presence of a high-velocity layer at 4.2-7.6 km depth beneath the Blue Ridge. Negative conversions are generated at the base of the high-velocity layer, and positive conversions are generated at the top. For station D18, the negative conversion at 5.9 km corresponding with the base of the high-velocity layer is evident, though the top of the layer is not imaged.

Figure DR3.

Positive conversions in receiver functions from stations along the Brevard zone (D17 and W31.5) and northwestern flank of the Inner Piedmont (D14 and W31) are indicative of an upward decrease in velocity marking the top of the high-Vs meta- sedimentary layer at 5-7 km depth, consistent with the interpretation that passive margin rocks dominated by dolostone and quartzite extend slightly southeast of the Brevard zone.

Figure DR4.

For station Z52A in the Inner Piedmont, positive and negative conversions in receiver functions from the northwestern and southern backazimuths, respectively, are indicative of a low-velocity zone at 6-10 km depth. Positive conversions are generated at the base of the low-velocity zone, and negative conversions are generated at the top. At station Y52A on the northwestern flank of the Inner Piedmont, the negative conversion at 10.2-km depth is interpreted to mark the base of the high-Vs platform sequence.

Figure DR5.

Positive conversions from stations across the Inner Piedmont corresponding with depths of 8.5-13.1 km are consistent with depths to Grenville basement determined from seismic reflection profiling (Hatcher et al., 2007).

Figure DR6.

Negative conversions in receiver functions across the Carolina terrane indicate an upward increase in velocity at depths of 5.9-12.7 km. For stations D03-D05, the conversions are interpreted to mark the base of high-Vs Carolina terrane arc rocks.

Earlier negative conversions from stations D05-D07 and Z53A are interpreted to mark velocity discontinuities associated with Alleghanian thrust sheet imbrication.

Figure DR7.

Positive conversions in receiver functions from stations D03 and D08 in the Carolina terrane are indicative of an upward decrease in velocity at depths of 4.7-5.1 km, reflecting the

complex internal structure of the Alleghanian thrust sheet.

Figures DR8-DR16.

Bootstrapped receiver-function stacks. In each figure, the mean stacked trace is shown with 2-sigma error bounds to demonstrate the robustness of the intracrustal P-SV conversions (arrows) used to estimate conversion depths in Fig. 4 (Figs. DR8-DR14) and Fig. 3 (Figs. DR15-DR16). For each set of stacked traces, the corresponding event backazimuth, Gaussian value, and number of the receiver functions included in the stack (N) are shown. The bootstrapping analysis is based on the method of Efron and Tibshirani (1991).

Figures DR8-DR14.

Bootstrapped receiver-function stacks for gathers shown in Figs. DR1-DR7.

Figures DR15-DR16.

Bootstrapped receiver-function stacks for stations D04 and W33 shown in Fig. 3.

Figure DR17.

Distribution of events used in the calculation of receiver functions.

Table DR1

Events used in the calculation of receiver functions for each station.

Table DR1: Events used in the calculation of receiver functions for each station

Event (yr/julian day/hr/min)	Latitude	Longitude	Station
2011.152.12.55	-37.57	-73.69	d17
2011.171.16.36	-21.68	-68.19	d08, d17
2011.175.03.09	51.98	-171.82	d05, d14, w30
2011.216.13.51	48.77	154.84	d05, d14, w30
2011.227.02.53	-1.81	-76.90	d17
2011.236.17.46	-7.65	-74.51	d08, d17
2011.245.10.55	52.10	-171.72	d05, d14, w29, w30
2011.245.13.47	-28.39	-63.06	d08, d17
2011.252.19.41	49.39	-127.06	d05, d14, w29, w30
2011.279.11.12	-24.13	-64.30	d08
2011.301.18.54	-14.44	-75.99	d08, d17
2012.030.05.11	-14.16	-75.62	d08, d17
2012.074.09.08	40.89	144.94	d14, w30
2012.085.22.37	-35.18	-71.79	d08, d17
2012.108.03.50	-32.63	-71.37	d08, d17, y52a, z52a, z53a
2012.135.10.00	-17.70	-69.57	d03, d08, d17, d18, d19, d22, y52a, z52a, z53a
2012.156.00.45	5.30	-82.58	d22
2012.171.15.56	53.36	171.59	z52a
2012.176.03.15	57.61	163.20	d03
2012.184.23.31	-14.41	-75.59	d22
2012.190.11.33	45.48	151.32	d03
2012.215.09.38	-8.41	-74.26	d03, d08, d17, d18, d19, d22, y52a, z52a, z53a
2012.223.18.37	52.63	-167.42	d03, z52a
2012.227.02.59	49.80	145.06	d03, d04, d05, d06, d07, d12, d14, d19, d20, d21 w29, w30, w31, w31.5, z52a
2012.270.23.39	51.61	-178.31	d03, d04, d05, d06, d07, d12, d14, d19, d20, d21 w29, w30, w31, w31.5, z52a
2012.274.16.31	1.92	-76.36	d03, d17, d18, d19, d22, y52a, z52a, z53a
2012.302.03.04	52.79	-132.10	d03, d04, d05, d06, d12, d14, d19, d20, d21 w29, w30, w31.5
2012.321.18.12	49.28	155.43	d03, d04, d05, d07, d19, d20, d21, w31

Table DR1 (continued)

Event (yr/julian day/hr/min)	Latitude	Longitude	Station
2013.005.08.58	55.39	-134.65	d03, d04, d05, d12, d14, d19, d20, d21 w29, w30, w31.5, z52a
2013.030.20.15	-28.09	-70.65	d03, d17, d18, d19, d22, y52a, z52a, z53a
2013.040.14.16	1.14	-77.39	d03, d17, d18, d19, d22, y52a, z52a, z53a
2013.045.13.13	67.63	142.51	d03, d04, d05, d07, d12, d14, d20, d21 w29, w30, w31, w31.5, z52a
2013.059.14.05	50.95	157.28	d03, d04, d05, d07, d12, d19, d20, d21
2013.109.03.05	46.22	150.79	d03, d04, d06, d07, d12, d14, d21, w29, w31, z52a
2013.139.18.44	52.34	160.07	d03, d04, d07, z52a
2013.144.05.44	54.89	153.22	d03, d04, d06, d07, d12, d14, d20, d21, w29, w31, z52a
2013.144.14.56	52.24	151.44	d12, d14, d20
2013.198.02.37	-15.66	-71.74	d03, d17, d18, d19, d22, w54a, x54a
2013.224.09.49	-5.40	-81.93	d03, d17, d18, d19, d22, w54a, x54a, y52a, z52a, z53a
2013.225.15.43	5.77	-78.20	d22
2013.235.08.34	-22.27	-68.59	z52a
2013.242.16.25	51.61	-175.36	d03, d04, d06, d07, d12, d14, d19, d20, d21 w29, w31, w31.5, z52a
2013.246.20.19	51.24	-130.40	d20
2013.247.02.32	51.59	-174.73	d03, d04, d07, d14, d19, d20, d21, w31.5, z52a
2013.258.16.21	51.58	-174.72	d03, d04, d06, d07, d12, d14, d19, d21, w31, w31.5, z52a
2013.268.16.42	-15.85	-74.56	d03, d17, d18, d19, d22, z52a, w54a, x54a, y52a, z53a
2013.274.03.38	53.20	152.79	d03, d04, d07, d12, d14, d19, d20, d21, w31, w31.5, z52a
2013.304.23.03	-30.29	-71.52	d22, z52a, w54a, x54a, y52a, z53a
2013.316.07.03	54.69	162.30	w31
2014.069.05.18	40.83	-125.13	w29
2013.074.23.51	-5.57	-80.97	d22, y52a
2013.075.21.16	-19.98	-70.70	d22, w54a, y52a, x54a
2014.081.12.59	-19.76	-70.87	d22, w54a, x54a
2014.082.18.20	-19.69	-70.85	d22
2014.091.23.46	-19.61	-70.77	d22, w54a, x54a

Table DR1 (continued)

Event (yr/julian day/hr/min)	Latitude	Longitude	Station
2014.093.01.58	-20.31	-70.58	d22
2014.093.02.43	-20.57	-70.49	d22, w54a, x54a
2014.094.01.37	-20.64	-70.65	d22
2014.114.03.10	49.64	-127.73	w29
2014.130.14.16	60.00	-152.13	w31
2014.235.22.32	-32.70	-71.44	w54a, y52a, x54a
2014.236.23.21	-14.60	-73.57	w54a, y52a, x54a

Figure DR1

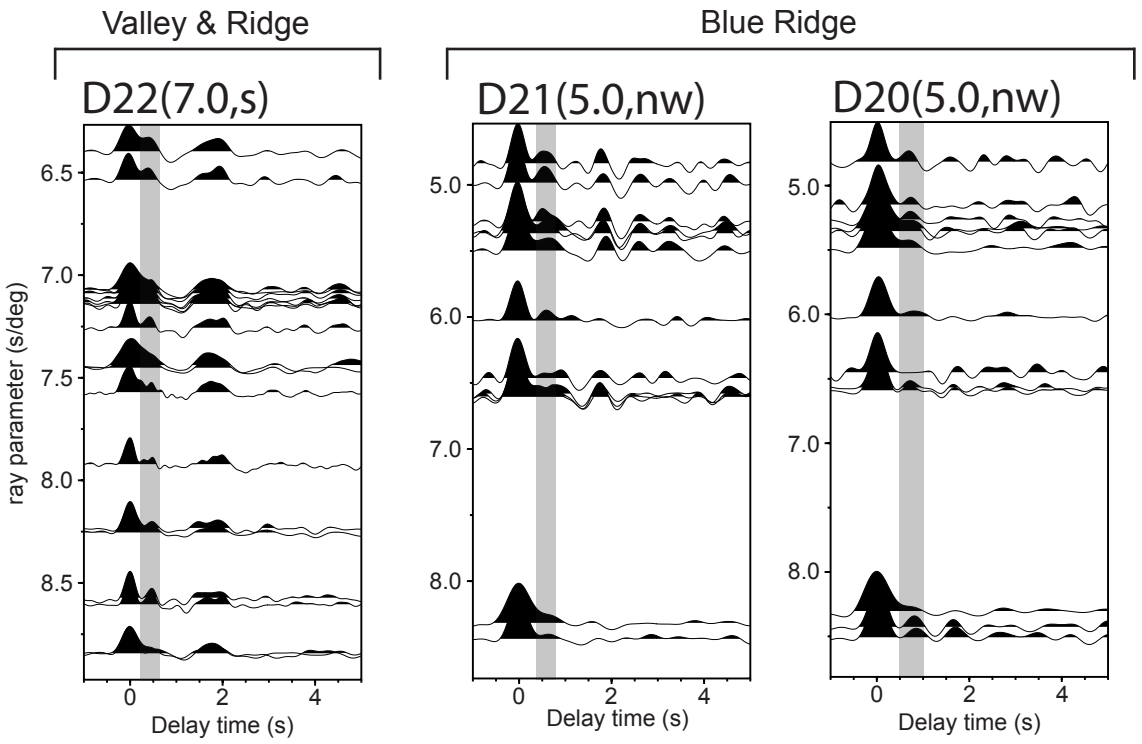

Figure DR2

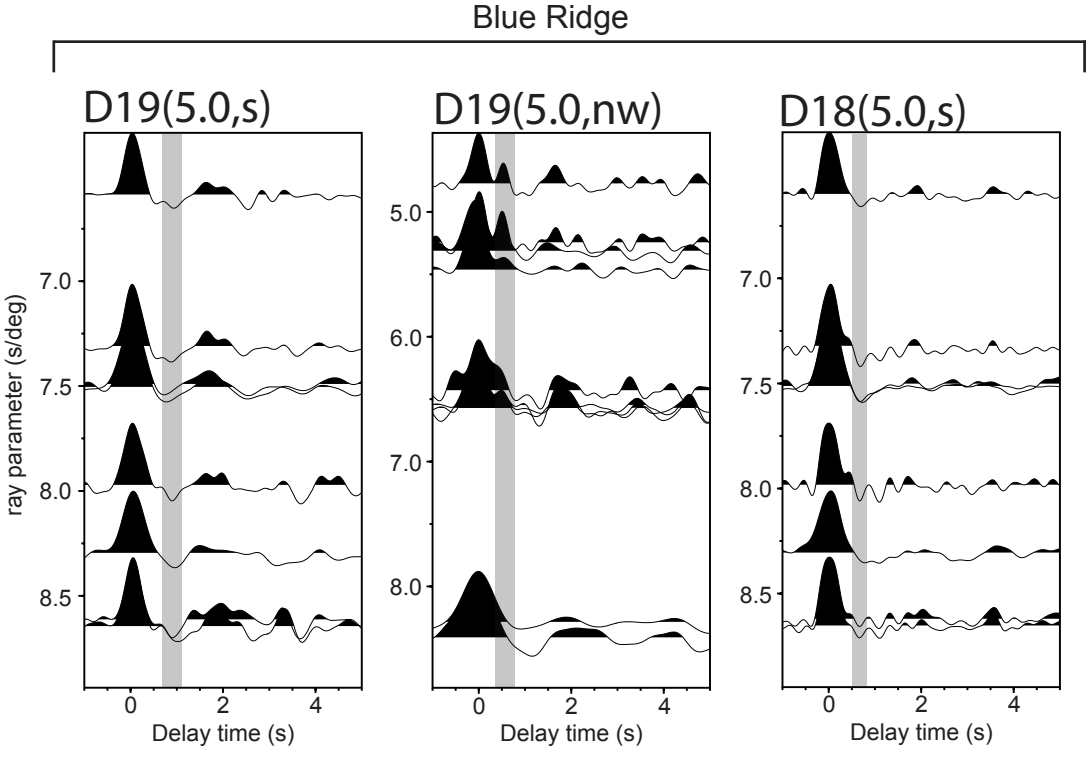

Figure DR3

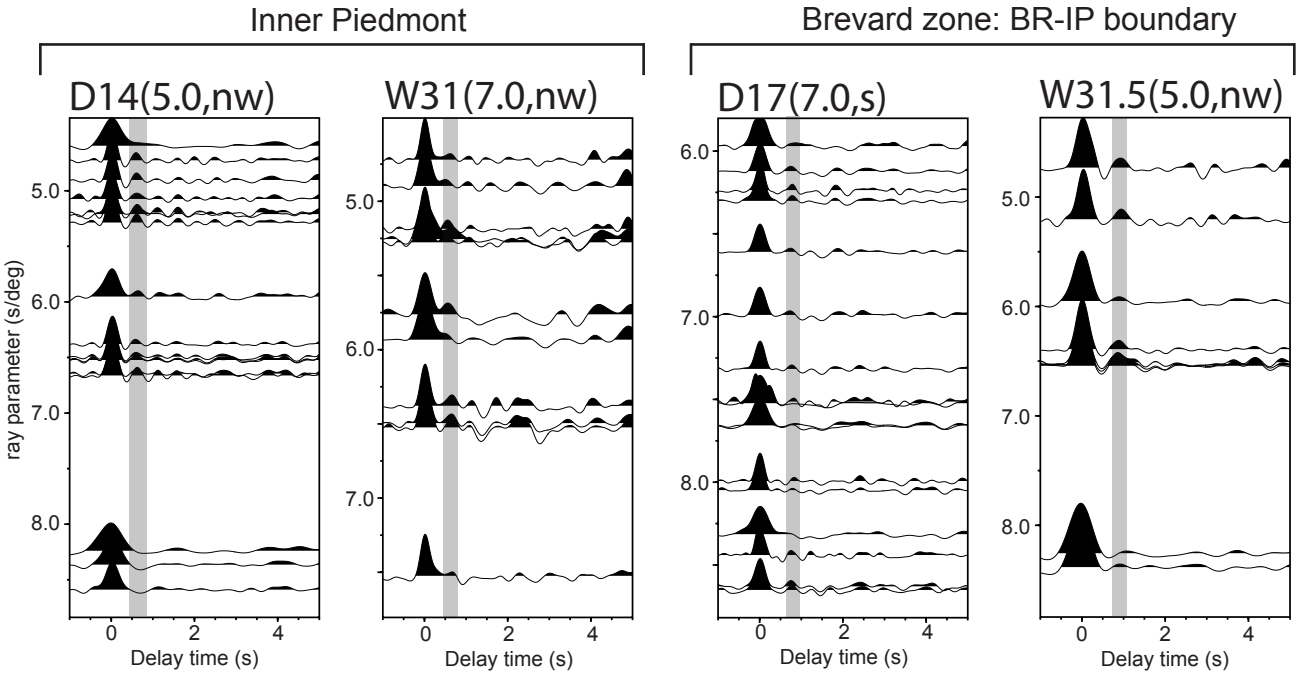

Figure DR4

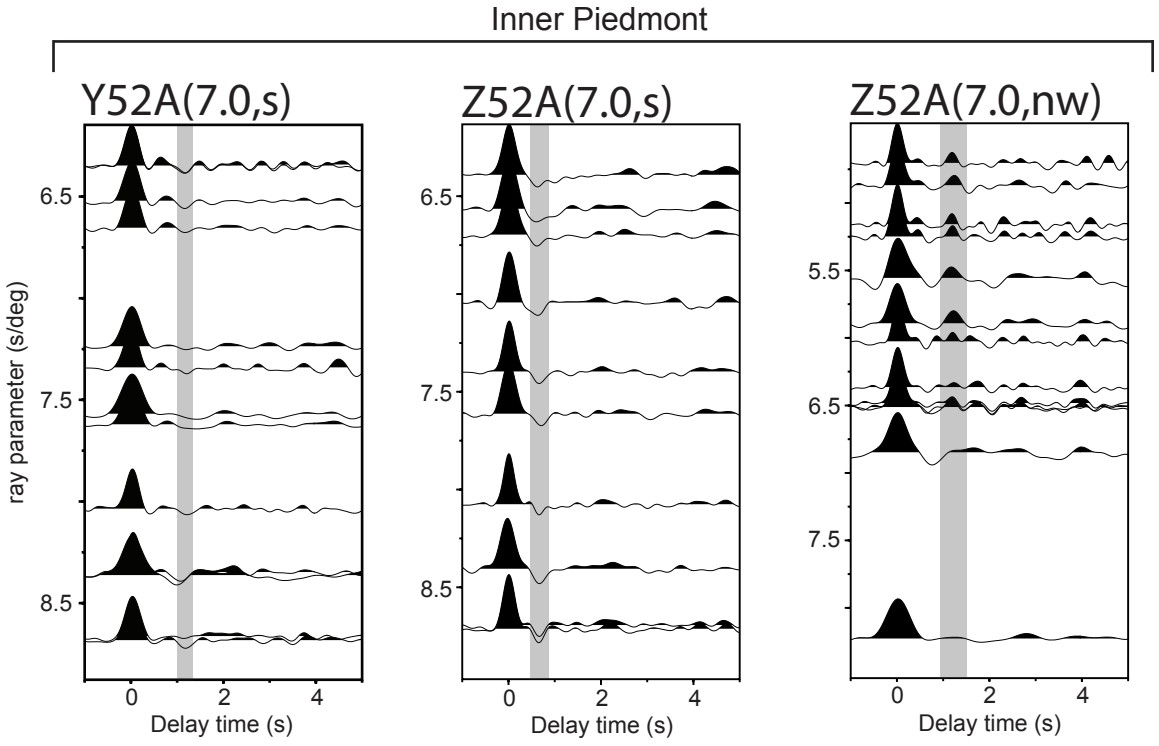

Figure DR5

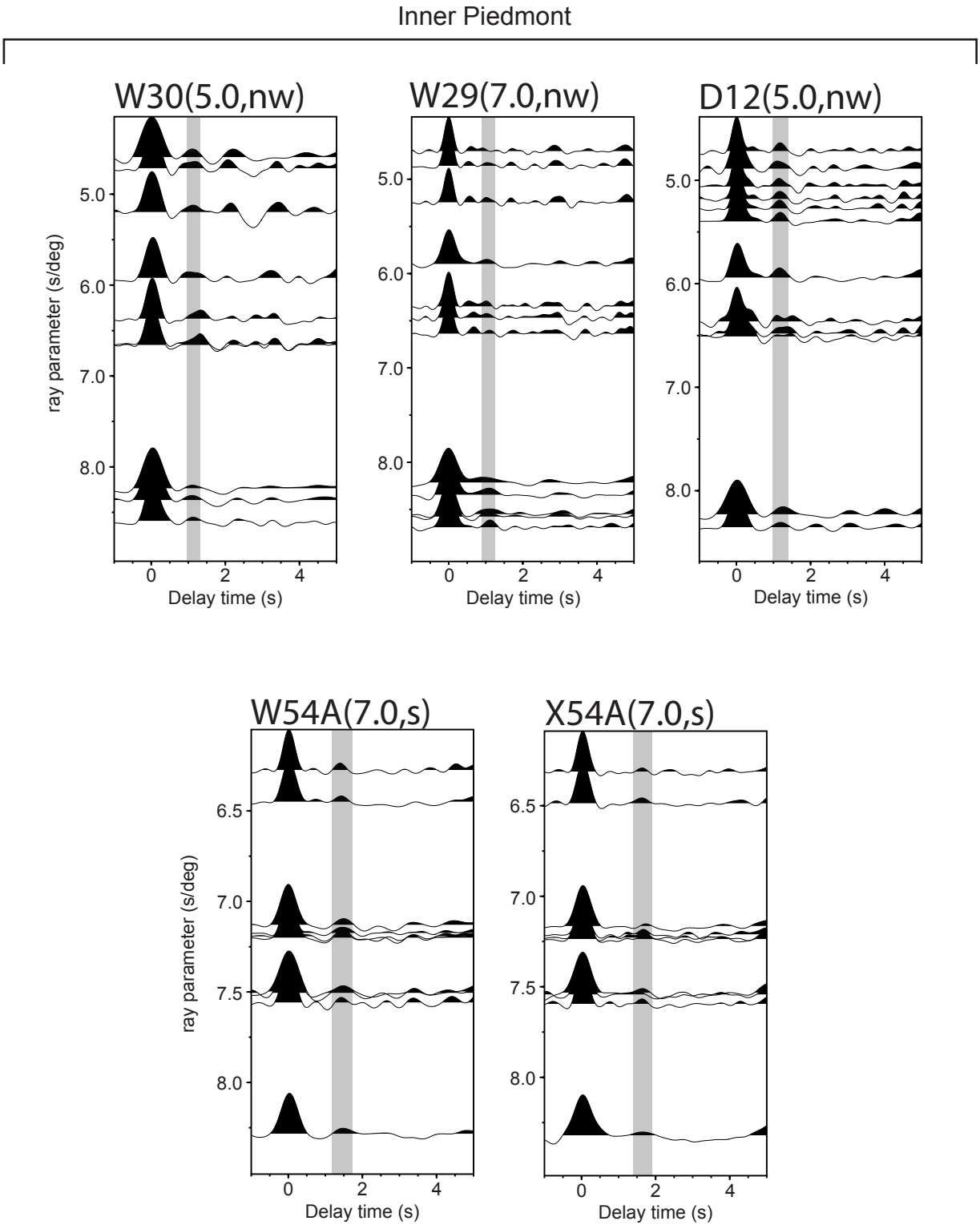
Inner Piedmont
W30(5.0,nw)
W29(7.0,nw)
D12(5.0,nw)
ray parameter (s/deg)
5.0
6.0
7.0
8.0
0
2
4
Delay time (s)
W54A(7.0,s)
X54A(7.0,s)
6.5
7.0
7.5
8.0

Figure DR6

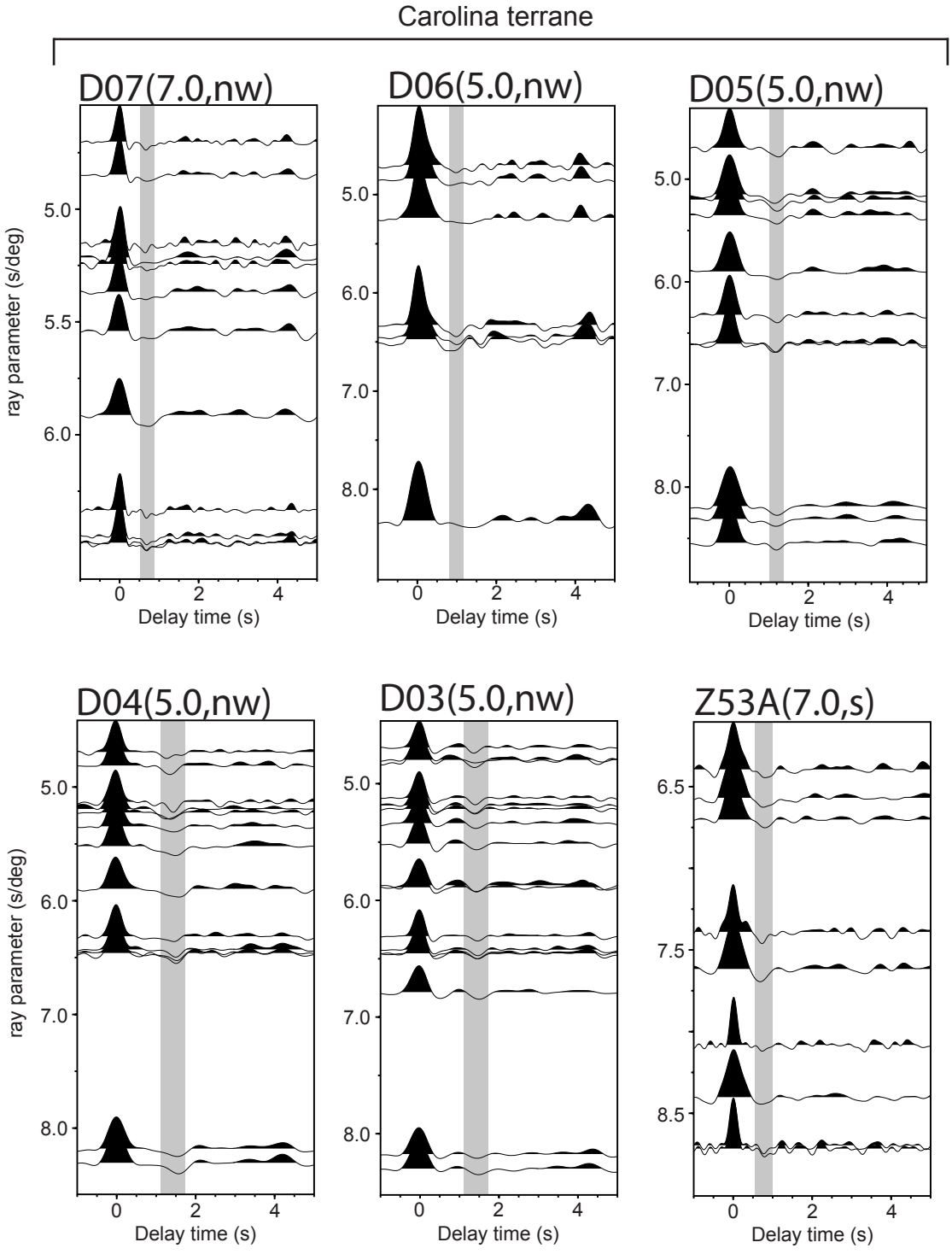
Carolina terrane
D07(7.0,nw)
D06(5.0,nw)
D05(5.0,nw)
D04(5.0,nw)
D03(5.0,nw)
Z53A(7.0,s)
ray parameter (s/deg)
Delay time (s)

Figure DR7

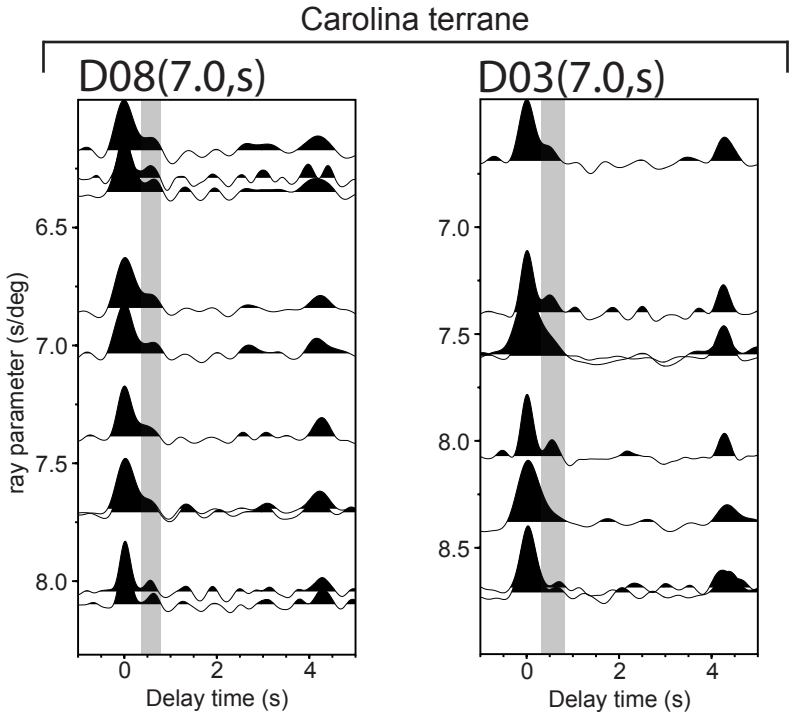
Carolina terrane
D08(7.0,s)
D03(7.0,s)
ray parameter (s/deg)
6.5
7.0
7.5
8.0
7.0
7.5
8.0
8.5
0
2
4
Delay time (s)
0
2
4
Delay time (s)

Fig. DR8

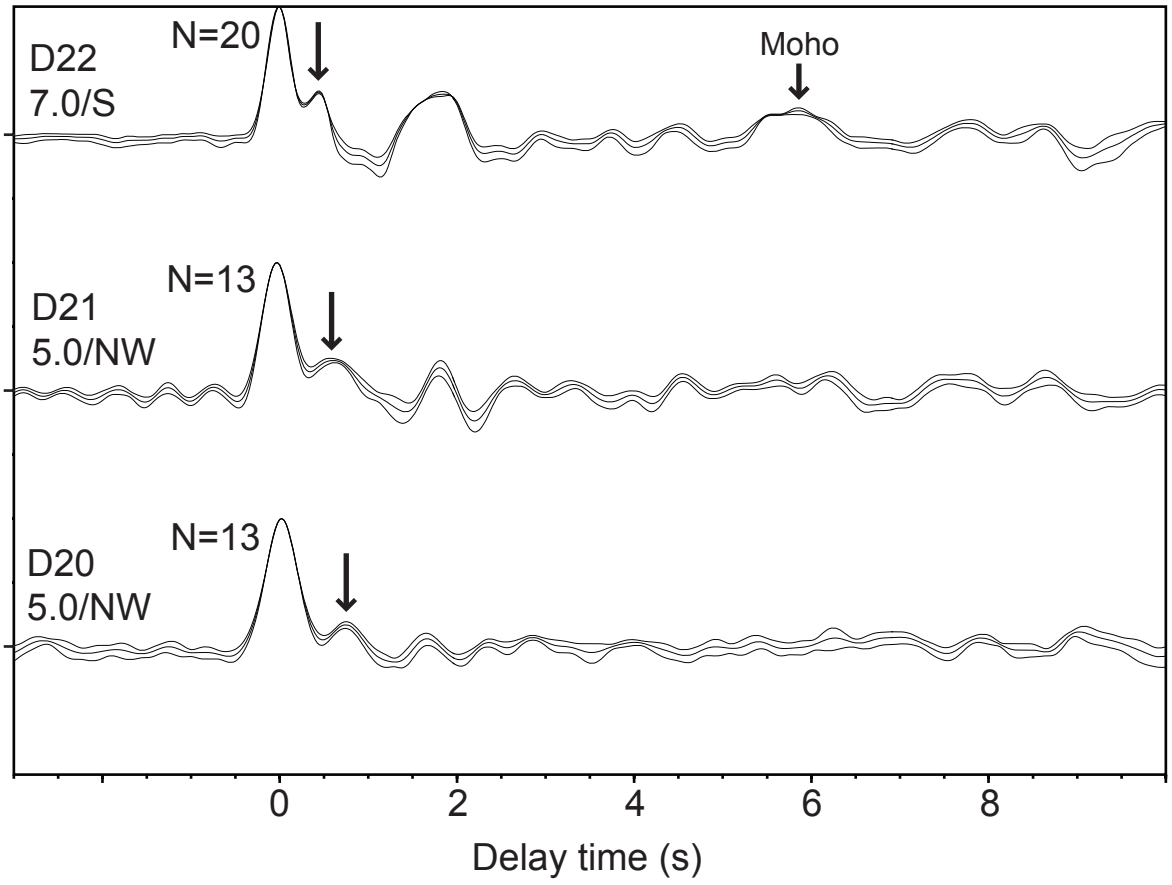

Fig. DR9

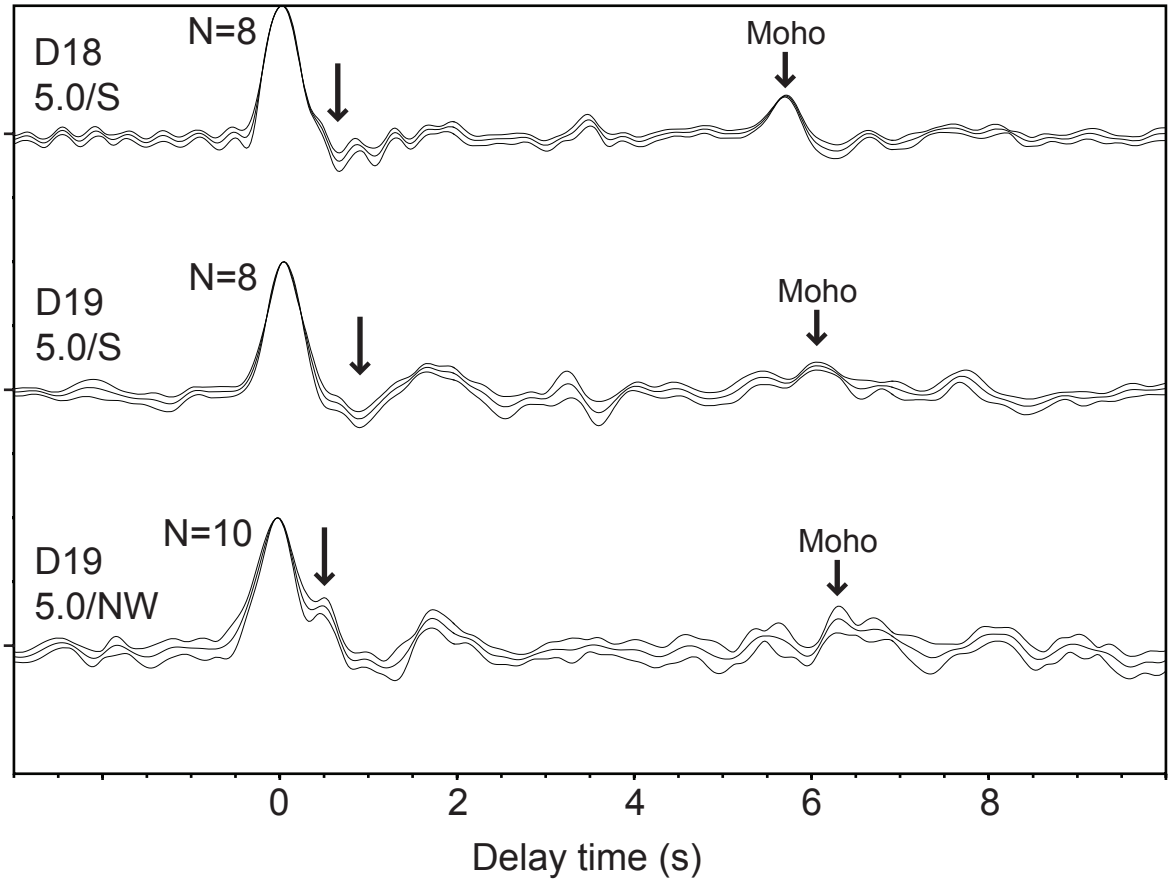

Fig. DR10

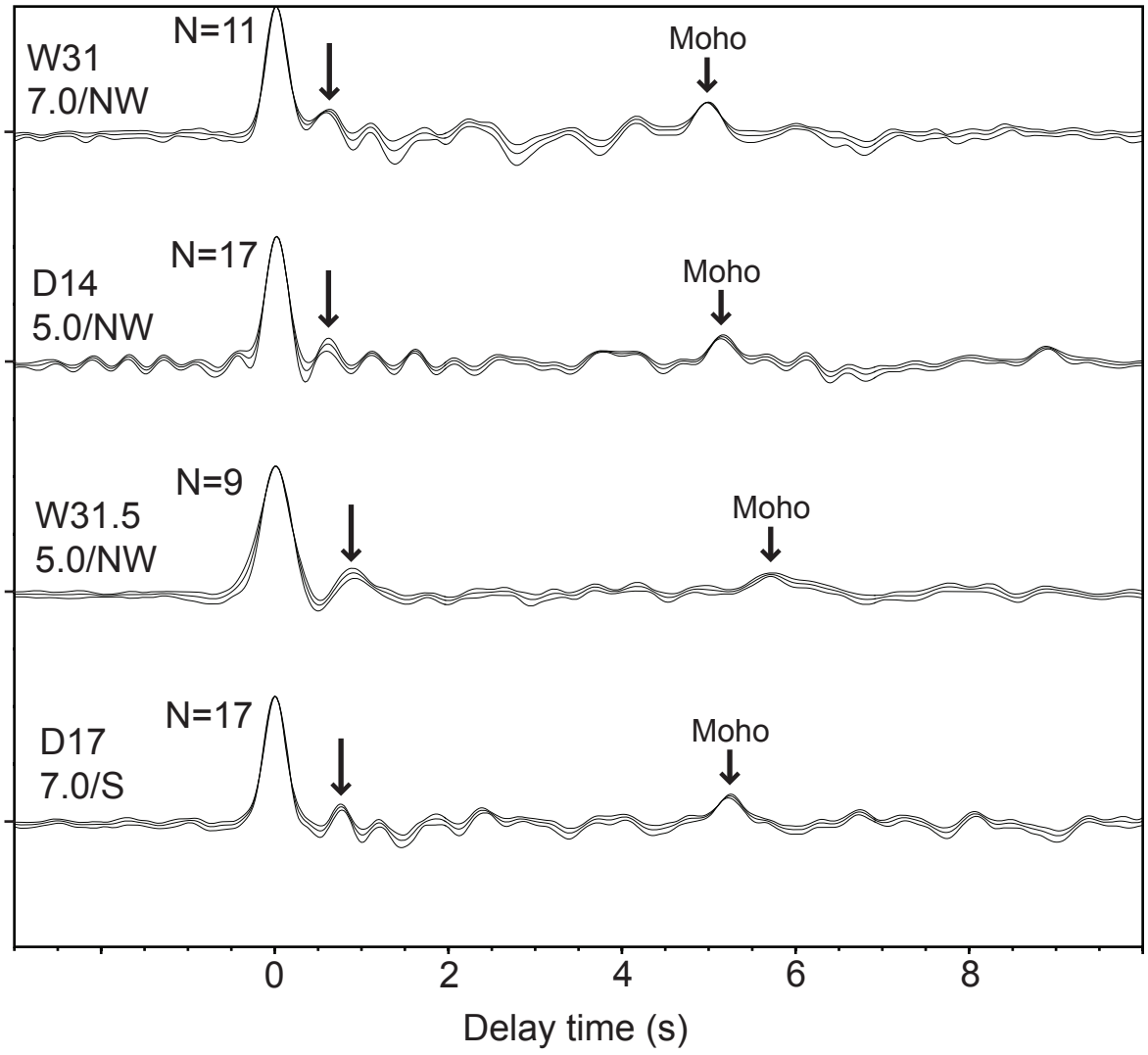

Fig. DR11

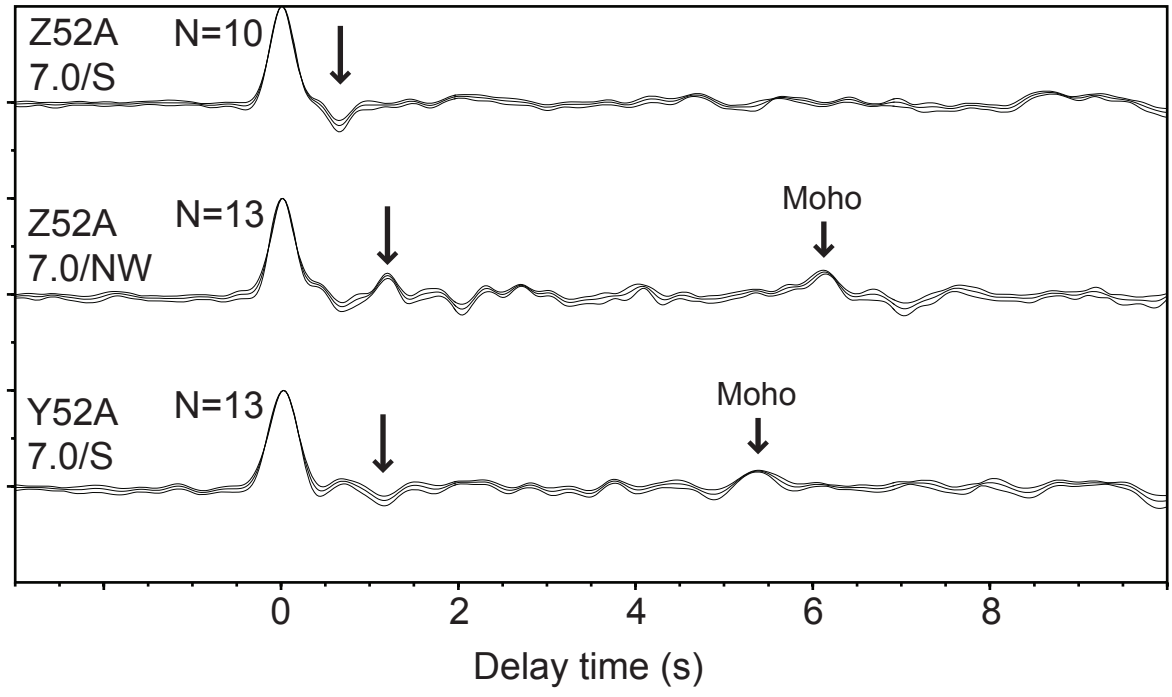

Fig. DR12

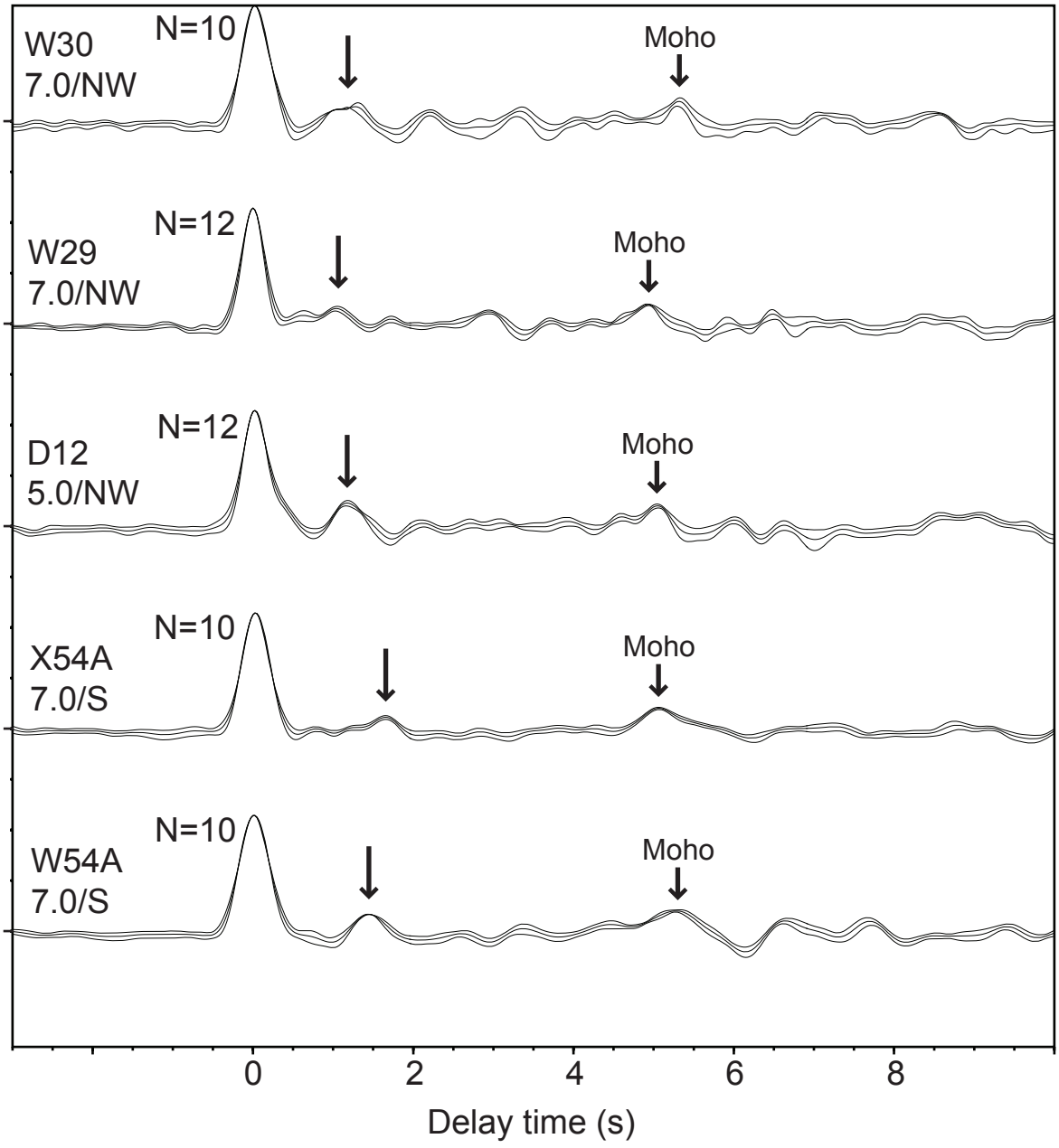
W30
7.0/NW
N=10
Moho
W29
7.0/NW
N=12
Moho
D12
5.0/NW
N=12
Moho
X54A
7.0/S
N=10
Moho
W54A
7.0/S
N=10
Moho
0
2
4
6
8
Delay time (s)

Fig. DR13

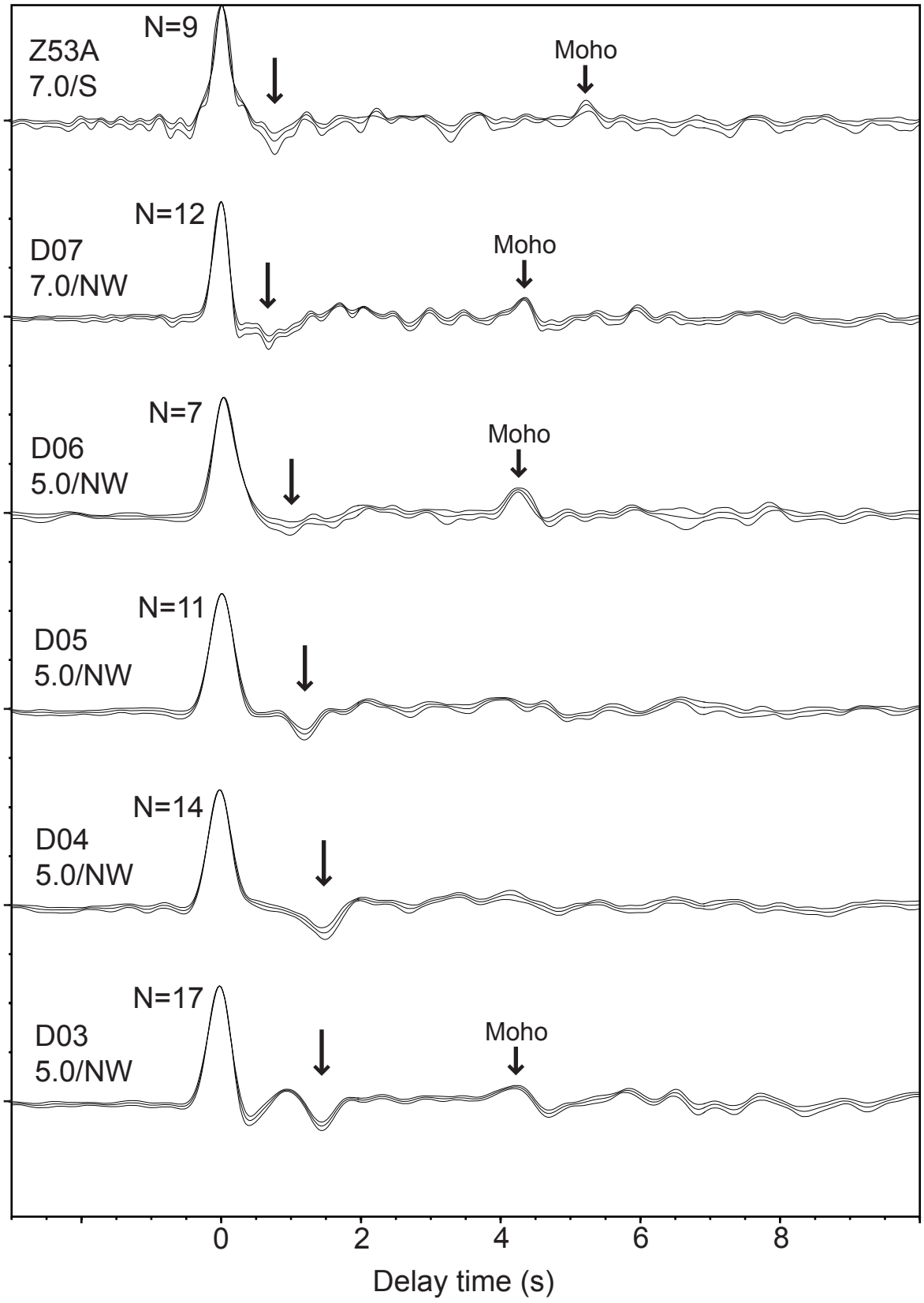
N=9
Z53A
7.0/S
Moho
N=12
D07
7.0/NW
Moho
N=7
D06
5.0/NW
Moho
N=11
D05
5.0/NW
N=14
D04
5.0/NW
N=17
D03
5.0/NW
Moho
0
2
4
6
8
Delay time (s)

Fig. DR14

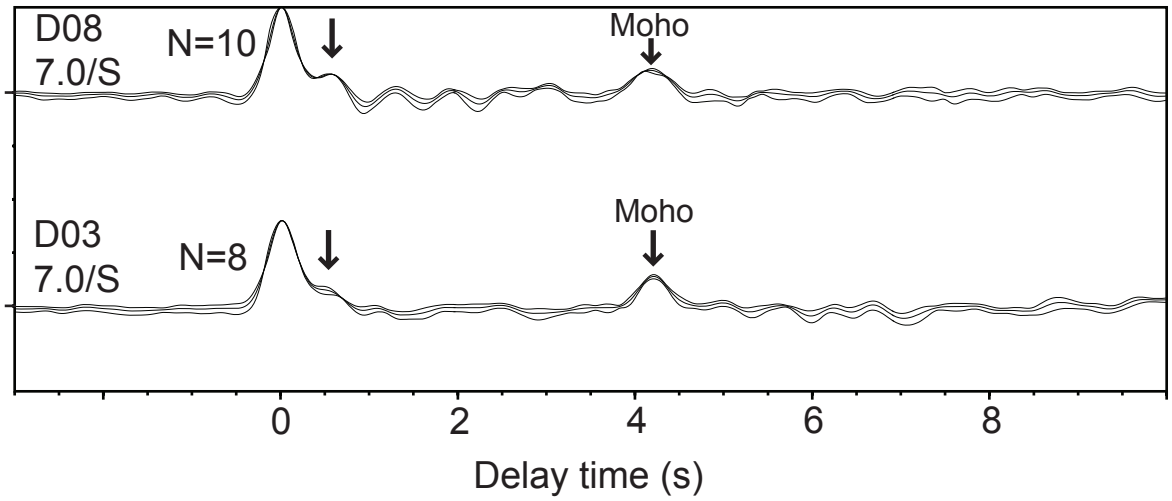

Fig. DR15

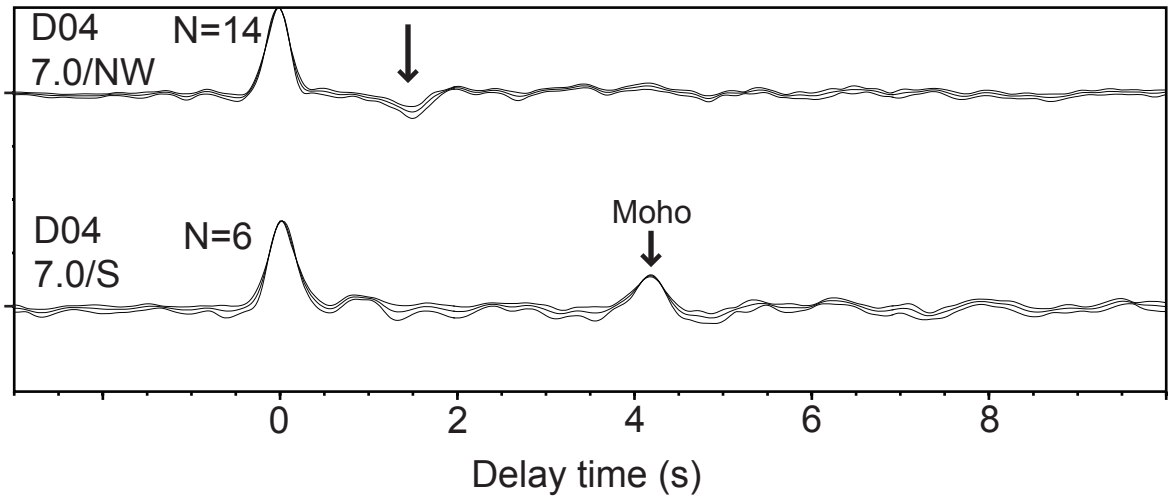

Fig. DR16

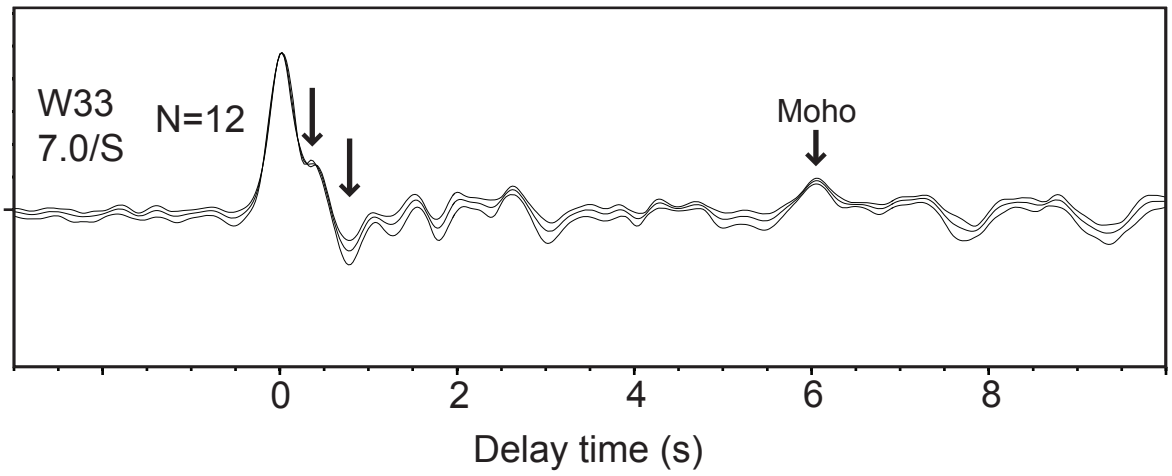

Fig. DR17